

Screening of seismic records to perform time-history dynamic analyses of tailings dams: a power-spectral based approach

Nicolás A. Labanda^{a,c,1}, Mauro G. Sottile^{a,b}, Ignacio A. Cueto^{a,b}, Alejo O. Sfriso^{a,b}

^a*SRK Consulting, Argentina.*

^b*Universidad de Buenos Aires. Facultad de Ingeniería. Buenos Aires, Argentina.*

^c*Curtin University, School of Earth and Planetary Science, Bentley, Western Australia, Australia.*

Abstract

Time-history deformation analyses of upstream-raised tailings dams use seismic records as input data. Such records must be representative of the in-situ seismicity in terms of a wide range of intensity measures (IMs) including peak ground acceleration (PGA), Arias intensity (AI), cumulative absolute velocity (CAV), source-to-site distance, duration, among others. No single IM is a sufficient descriptor of a given seismic demand (e.g. crest settlement) because different records, all of them compliant with any IM, can produce a very wide range of results from insignificant damage to global failure. The use of brute force, where hundreds of seismic records compliant with a set of IMs are employed, has proven to be a reasonable workaround of this limitation, at least as it is able to produce a probabilistic density function of demand indicators. This procedure, however, requires a large number of runs, and is therefore expensive and time-consuming. Analyses can be optimized if an a priori simple tool is used to predict which seismic records would yield a given demand, thus obtaining estimations with much fewer runs. In order to perform a more precise selection, a semi-analytical screening procedure is presented in this paper. The procedure makes use of the spectral properties of the seismic record, considering only the intensity of the frequency content which is not filtered by the dam to obtain an a priori estimate of demand, expressed in this case in terms of displacements. The tool is validated using analytical and numerical models that prove insensitivity to the constitutive model used in the analysis, and is applied to a large tailings dam subjected to strong earthquakes.

Keywords: Liquefaction, Tailings dams, Earthquake, Deformation analysis

*Corresponding Author at: Curtin University, Bentley, Western Australia, Australia (nlabanda@fi.uba.ar).

1. Introduction

Tailings are mine residues in the form of rock flours. They are generally deposited hydraulically as a viscous mixture into storage facilities (TSFs). The lack of post-deposition compaction results in loose states, which can be locked as such by chemo-electrical interactions among the particles and early diagenesis [1]. The storage facility construction method can be downstream, centerline or upstream, named after the crest movement direction during the raise. Upstream-raised dams are highly attractive from an economic point of view as they minimize construction volumes; however, they are the least safe, as stability largely relies on the strength of the tailings themselves. Recent massive failures of upstream-raised TSFs (such as Merriespruit, Samarco and Brumadinho [2]) have depicted their vulnerability against liquefaction. Upstream-raised TSFs have an annual probability of failure five to ten times larger than hydroelectric dams [3].

According to Rico et al. [4], liquefaction is one of the main causes of tailings dams failures, with dynamic liquefaction representing around 15% of the cases. Liquefaction occurs when loose water-saturated tailings undergo an increase of pore pressure and loss of strength due to undrained shearing or internal fabric collapse. In the context of static liquefaction, due to the difficulty of preventing and predicting events that might trigger the failure, guidelines used as international best practice (e.g. [5]) recommend to assume that triggering will occur during the lifetime of the TSF and then perform limit equilibrium (LE) analyses adopting a fully-softened shear strength. The safety factor required for such analysis is set close to 1.0 [5]. While safe, this approach makes no allowance for the amount of strain required for a given dam to reach a point of uncontrolled progressive failure [6]. This approach is reasonable to design new TSFs but it falls short in assessing the risk posed on existing TSFs, both operating and abandoned.

Liquefaction imposed by seismic loading is generally not analyzed as a process [7]. Instead, the risk of liquefaction is estimated based on the (static) brittleness of the tailings. If the material is deemed liquefiable, static stability analyses considering post-seismic undrained shear strength are performed, without considering inertia effects at all. This is a very limited approach, producing essentially the same design regardless of the seismicity of a given site. In this sense, numerical time-history deformation analyses become imperative to better understand the dynamic liquefaction vulnerability of a given dam and to warrant that the designed freeboard is adequate.

One of the crucial aspects of dynamic liquefaction assessments is the selection of a proper and representative set of seismic records as input for the time-history deformation analyses. Several ground motion intensity measures (IMs) have been proposed to characterize the destructive potential of a record: peak ground velocity (PGV) and peak ground acceleration (PGA) are the most widespread but limited IMs [8]; Arias intensity (AI), proportional to the total energy content of the signal [9]; modified cumulative absolute velocity (CAV and CAV5), the latter being the integral of the acceleration after

application of a 5 cm/s^2 acceleration threshold [10]; a normalized hysteretic energy, an empirical relation between dissipated shear energy and residual excess pore pressure ratio [11], among many others.

In the context of liquefiable soils, new approaches have been proposed recently. Kramer et al. [12] review procedures to detect the time of liquefaction triggering, comparing their performance with empirical methods. The research is focused on signal analysis using short-term Fourier transform (STFT), spectrograms, wavelets transforms and Stockwell spectrum procedures, showing that the mean frequency content tends to reduce in signals recorded above a liquefied stratum [13, 14, 15].

Motivated by its simplistic and computationally efficient model, other researchers have used sliding-block Newmark-type models [16] to estimate settlements of slopes under shaking, and adopting empirical modifications of the Arias intensity to characterize the excitation [17]. Combinations of Newmark-type models, as a displacement estimator, and some selected IMs like PGA, CAV and AI, are popular in hazard analysis in geotechnics [18, 19, 20, 21, 22].

Due to the improvement of computational capacity, numerical methods are progressively replacing analytical models. Naeini et al. [23] addressed the problem of tailings dams subjected to dynamic loads by focusing on detecting resonance points by means of transfer functions [24, 25]. Jin et al. [26] proposed a theoretical framework for mudslides based on experimental and numerical models, pointing out that instability mechanisms are somehow similar, relating an appropriate design of a tailings dam to the site seismicity rather than to its construction procedure. It is worth noting that computational models have become the standard procedure to perform forensic studies over real dam failures, and some remarkable works are recommended as a reference [27, 28, 29, 30]. Despite advances in this subject matter, tailings engineering keeps using correlations of engineering demand parameters with classical IMs, usually leading to highly scattered results [31].

This paper presents a generalization of Arias Intensity (AI) based on the spectral properties of the input signal and it uses it as a tool to produce a preliminar estimate of the seismic demand of any given earthquake. The use of the tool is validated using classical/analytical methods and dynamic numerical models of a large TSF, and the correlation between this new IM and the maximum displacement during time-history analyses is shown in this case, comparing its performance with the results obtained with classical IMs.

The paper starts describing an example of a time-deformation analysis of a TSF in Section 2, that will be used to show the strength and consistency of the proposal. In Section 3 the constitutive model PM4Sand, used for subsequent numerical liquefaction assessment, is calibrated using laboratory and field tests. In Section 4, the proposed IM based on spectral power is presented in detail. Numerical results related to deformation induced by pore pressure buildup are presented and discussed in Section 5, and the predictive capability and efficiency of the tool is tested. Finally, some conclusions and outlooks are drawn in Section 6.

2. Deformation analysis of a TSF

2.1. Description

As an example, the process for the deformation modeling of a TSF is shown. The TSF considered is an upstream-raised facility located in a region with high seismicity. It has a current approximate height of 70 *m*; an additional raise of 10-15 *m* is expected to be deposited in the next few years. The facility consists of a starter dam, embankment raises forming a 3H:1V slope; a sandy silt/silty sand loose tailings body; and a reinforcement buttress built at the toe. The combination of loose tailings and high seismicity results in a high risk of liquefaction, should the tailings be near saturated or saturated. A schematic cross-section of the TSF in its final configuration is presented in Figure 1. This is a fairly large installation where the value of numerical deformation modeling is apparent.

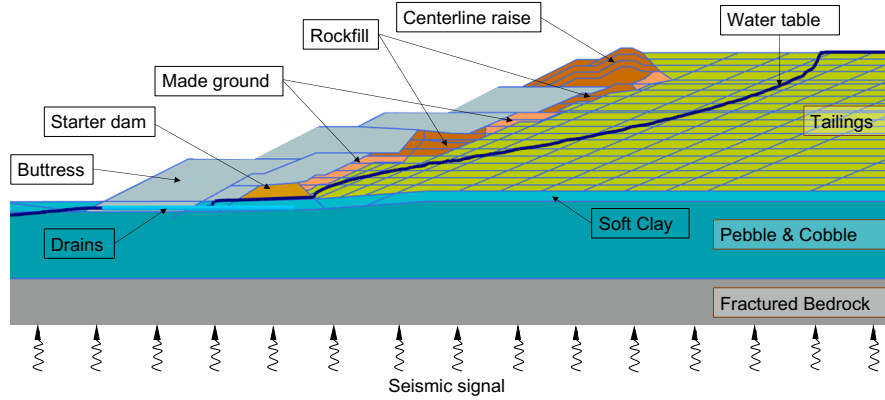


Figure 1: TSF considered in the paper and its geotechnical units.

2.2. Numerical model

A numerical model must be set-up and many runs must be carried out in order to estimate the seismic demand of the TSF or, in other words, the required freeboard and the need of a reinforcement buttress. In this section, a brief description of the numerical model used in this example is presented.

2.2.1. Mesh and boundary conditions

The model is generated in Plaxis 2019 finite element software. The mesh has 12281 6-node triangular elements with an average size of 2.8 *m*, a maximum size of 27.27 *m* and a minimum size of 0.18 *m*.

Far field boundary conditions are used at the left and right boundaries. A compliant base is employed, where horizontal acceleration time signals are introduced as input at the bottom for the dynamic modeling. For simplicity, no vertical accelerations are considered in this study.

2.2.2. Constitutive models

HS-Small model is used to simulate the construction sequence of all materials other than the bedrock, where linear elasticity is employed. Once the final configuration is reached, HS-Small model is changed to PM4Sand model only for the tailings. Immediately before the application of the time-history ground motions, a nil-step is performed to assure a fully converged state prior to the dynamic analyses.

It is worth noting that HS-Small model is preferred to simulate the construction stages in order to overcome the limitations of the PM4Sand model when dealing with monotonic compression stress paths and to produce a realistic stress-field in the dam body, relevant to the dynamic response of the dam. An insight of the model calibration is provided in the next section.

2.2.3. Construction sequence

Figure 2 shows the construction sequence that is used to simulate the staged construction prior to the dynamic deformation analyses. During the dam rise, the deposition of each layer modeled using subsequent consolidation-type stages, allows excess pore pressure generation and dissipation. After reaching the final configuration, a full consolidation of excess pore pressures is allowed, since the design earthquake will take place after a recurrence period of 7500 years, following ANCOLD guidelines [5].

2.2.4. Rayleigh damping

Rayleigh damping is required to account for the small-strain damping, which is not captured adequately by both, HS-Small and PM4Sand models. To determine Rayleigh damping, the fundamental frequency of the tailings body is computed as:

$$f_1 = \frac{V_{s,av}}{4H} \quad (1)$$

where $V_{s,av}$ is the average shear wave velocity in the tailings body, f_1 is the fundamental frequency of the system and H is the maximum height of the TSF. Far behind the crest of the slope, the mean pressure at mid-height of the TSF is approximately 200 kPa . Using the parameters introduced in Section 3, the average shear modulus is:

$$G_0 = G_0^{ref} \left(\frac{p}{p_{ref}} \right)^m = 45 [MPa] \left(\frac{200 [kPa]}{100 [kPa]} \right)^{0.75} = 75 [MPa] \quad (2)$$

which translates into an average shear wave velocity of $V_{s,av} = 200 \text{ m/sec}$ and a natural frequency of about 0.70 Hz . If the same calculation is done at the crest of the final elevation, the fundamental frequency is approximately 0.90 Hz . Therefore, the expected range of the tailings natural frequency is from 0.70 to 0.90 Hz . At the buttress, the first natural frequency mode is estimated to be

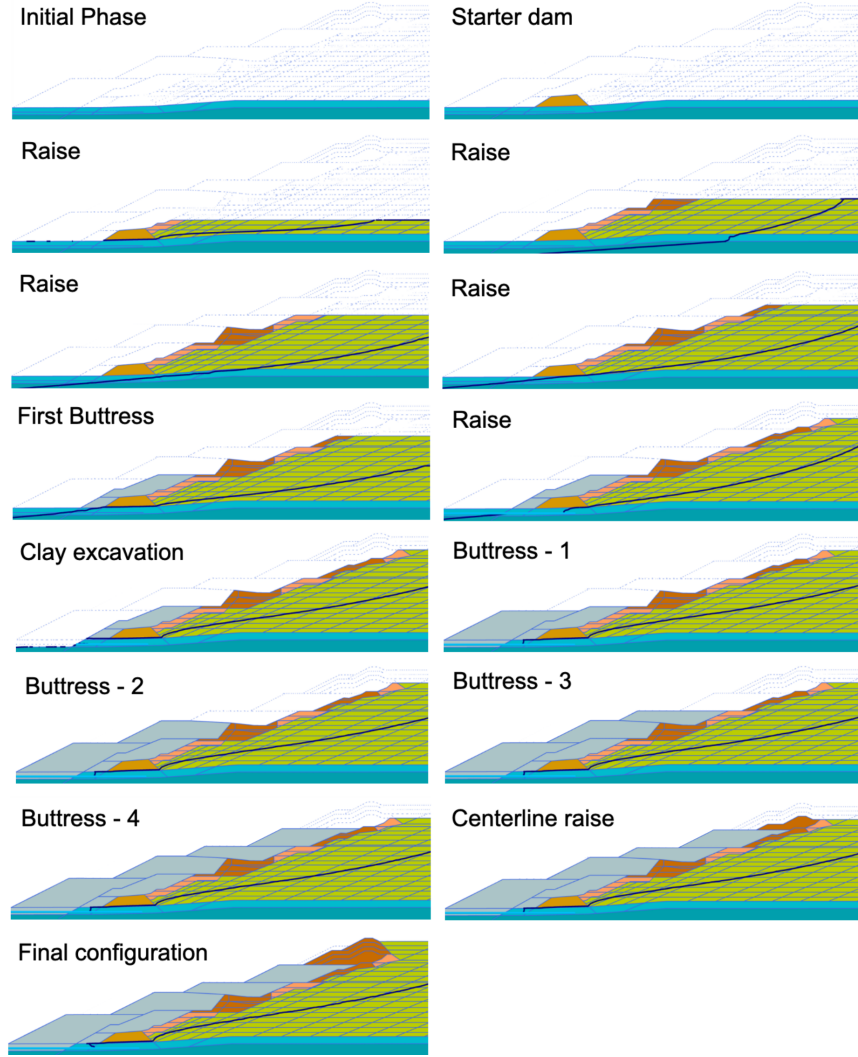


Figure 2: Simulation of dam construction and raises.

approximately $2.5Hz$. In addition [32], an upper bound target frequency f_2 should be:

$$f_2 = \frac{f_{fund}}{f_1} \quad (3)$$

where f_{fund} is the fundamental frequency of the signal, being $4 Hz$ the most representative value for the considered set of seismic records. Then, the upper bound target frequency is about $5 Hz$ for an average tailings first natural

frequency mode of 0.80 Hz . In this case, values adopted for the Rayleigh coefficients α and β are 0.04189 and 0.00212 respectively, so that: the damping is 1% from 0.4 to 1.0 Hz , 1.0 to 2.0 % for frequencies from 1.0 to 3.0 Hz , and 2.0 to 3.0 % for frequencies from 3.0 to 5.0 Hz , which is the estimated upper bound. This is aligned with Ref. [33].

3. Constitutive models calibration for tailings

The mechanical behavior of the tailings material has been characterized by means of laboratory and field testing. Full details of isotropically consolidated drained and undrained triaxial compression tests (CIDC /CIUC) results can be found in Ref. [34]. In addition, the authors provide the calibration of NorSand model, along with numerical cavity expansion analyses and inverse interpretation of the state parameter along a similar cross-section of the TSF using CPTu data (after Ref. [35]). The calibration of the NorSand model parameters is presented for a fine and coarse tailings sample, named Sample A and B, respectively. Table 1 shows a summary of the parameters that define the Critical State Line (CSL) according to the expression shown in Eq. (4). Given the tailings complex deposition sequence, an average CSL is used in this study.

$$e_c = \Gamma - \lambda_{10} \cdot \log p' \quad (4)$$

Table 1: Critical state line parameters.

Sample	Γ	λ_{10}	e_{min}	e_{max}
Sample A	1.02	0.170	0.285	1.218
Sample B	1.12	0.175	0.229	1.114
Average	1.07	0.172	0.257	1.166

The PM4Sand model calibration strategy is summarized as follows: i) the average NorSand CSL is converted from $e - \log p'$ to $D_r - \log p'$ space using the average minimum and maximum void ratios, e_{min} and e_{max} respectively; ii) the PM4Sand parameters that define the CSL, Q and R , are adjusted to approximate to the NorSand CSL within a representative stress range; iii) the contraction rate parameter (h_{p0}) is calibrated using two available cyclic direct simple shear tests (CDSS); iv) a representative relative density (D_r) is computed at different sub-regions of the TSF to reflect the in-situ state of the material, as a function of the mean effective stress (p') before the earthquake and the already interpreted state parameter (ψ). The remaining PM4Sand parameters are adopted with default values proposed by Ref. [36].

A comparison between the averaged NorSand model and the calibrated PM4Sand model CSL is shown in Figure 3. The calibration of PM4Sand Q

and R parameters aims to approximate the NorSand model CSL to the range of stresses that are of interest for this study, which varies from 50 to 600 kPa . Values of $Q = 11.8$ and $R = 3.9$ are obtained; as shown in Figure 3, the matching is acceptable.

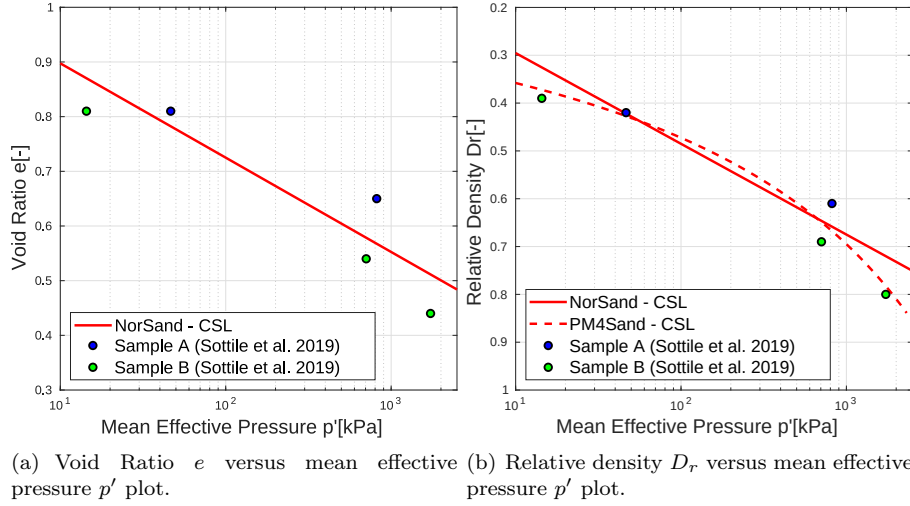


Figure 3: Critical State Line (CSL) calibration and comparisons with isotropically consolidated undrained and drained tests.

Two Cyclic Direct Simple Shear tests (CDSS) were performed on the coarser tailing (Sample B). The results are shown in Figure 4 and are summarized as follows: i) Test 1 entails an initial vertical effective stress of $\sigma'_v = 200$ kPa and an initial void ratio of $e_0 = 0.642$; for a Cyclic Stress Ratio $CSR = 0.12$, 30 cycles were needed to fail the sample (defined as shear strain of 3.75%); ii) Test 2 had $\sigma'_v = 200$ kPa and $e_0 = 0.523$, corresponding to a denser state than Test 1; for $CSR = 0.12$, 69 cycles were needed to results in failure. It must be noted that the initial configuration for both tests entails negative state parametes, ranging from -0.10 to -0.20 approximately; therefore, for looser configurations, a lower amount of cycles for a given CSR is expected in order to reach failure. Elemental CDSS tests were performed using PM4Sand model and compared with the available test, from which a conservative value $h_{p0} = 0.75$ is determined. A summary of the PM4Sand parameters is shown in Table 2.

After calibrating all the PM4Sand model parameters, a representative relative density is determined at each region of the TSF model. Figure 5 shows the details of this procedure, which is summarized as follows: 1) the mean effective stress distribution at the TSF is obtained before the earthquake event, and an average value is computed at each soil cluster of the model; 2)

Table 2: PM4Sand model parameters for tailings, used in dynamic stages.

	Unit	Parameters
γ_{sat}	kN/m^3	18.0
G_0	-	450
h_{p0}	-	0.75
p_{ref}	kPa	103
e_{max}	-	1.166
e_{min}	-	0.257
n^b	-	0.50
n^d	-	0.10
ϕ'_{cv}	$^\circ$	32
ν	-	0.20
Q	-	11.8
R	-	3.4
k	m/s	1×10^{-7}

the state parameter is interpreted using CPTu data (after Ref [31]) and four different regions of constant ψ are defined: 0.000, 0.025, 0.050 and 0.075 ; 3) using the mean effective stress at each soil cluster and the assigned state parameter, a relative density is computed using the equation

$$D_r = \frac{e_{max} - (e_c + \psi)}{e_{max} - e_{min}}, \quad (5)$$

where e_c is the void ratio at the critical state line for the mean effective stress p' average over the soil cluster; 4) using a Python script, a PM4Sand material with a proper relative density is generated for each region of the model and assigned respectively. On the other hand, Table 3 presents the parameters of HS-Small model used for the dam raising and validation of the proposed seismic selection method. For the sake of brevity, the calibration of HS-small model is not presented here.

4. A priori estimator for the demand of seismic records

This section represents the core of the paper where, first, an intensity measure which is a generalization of Arias Intensity based on spectral power is mathematically defined and then, calculations are performed to a set of seismic signals and the proposed IM is determined for each earthquake.

4.1. Definition of an intensity measure based on spectral power

Calculations to obtain the spectral power content of a seismic signal are based on the Fast Fourier Transform (FFT), an efficient implementation of the

Table 3: HS-Small parameters for tailings, used in static stages.

	Unit	HS-Small
γ_{sat}	kN/m^3	18.0
ϕ'	$^\circ$	32
c'	kPa	0
ψ	$^\circ$	0
G_0^{ref}	MPa	45
$\gamma_{0.7}$	-	10^{-4}
E_{ur}^{ref}	MPa	60
E_{50}^{ref}	MPa	5
E_{oed}^{ref}	MPa	9
m	-	0.75
ν_{ur}	-	0.20
OCR	-	1.00
K_0^{nc}	-	0.50

Discrete Fourier transform (DFT). The formulation is stated in a discrete space, in order to explain the physical aspects more clearly.

Let $\{\mathbf{a}_n\} = a_0, a_1, \dots, a_{N-1}$ be a finite set of N elements uniformly spaced of time-history accelerations, the DFT is defined by means of Euler's formula:

$$\begin{aligned} \mathcal{F}\{\mathbf{a}_n\}(k) &= \{\mathbf{A}_k\} = \sum_{n=0}^{N-1} a_n \cdot e^{-i2\pi k \frac{n}{N}} \\ &= \sum_{n=0}^{N-1} a_n \cdot \left[\cos\left(\frac{2\pi}{N}kn\right) + i \cdot \sin\left(\frac{2\pi}{N}kn\right) \right] \end{aligned} \quad (6)$$

where $\{\mathbf{A}_k\}$ is a set of complex vectors which represents the amplitude and phase of a complex sinusoidal component and k an integer representing the frequency domain.

The power spectrum density in terms of the frequency is defined as

$$S_{xx}(k) = \|\mathcal{F}\{\mathbf{a}_n\}(k)\|^2 \quad (7)$$

while the total spectral power of the signal is expressed as

$$P_{0-\infty} = \sum_{k=0}^{\infty} S_{xx}(k) \Delta k \quad (8)$$

with Δk being the frequency sampling. In this paper, the seismic intensity measure used is a windowed version of the spectral power expressed in equation (8), where the highest frequency considered for the calculations is the limit of power accumulation i.e., $P_{0-X Hz}$ is the accumulated power between the frequencies 0 to $X Hz$. It is worth noting that, due to Parseval's Theorem

$$\sum_{n=0}^{N-1} \|a_n\|^2 = \sum_{k=0}^{\infty} \|\mathcal{F}(k)\|^2 \quad (9)$$

which means that, when the considered power spectrum is computed considering the full frequency domain, the intensity measure expressed in terms of the spectral decomposition tends to represent classical intensity measures based on the integration of the seismic signal such as the Arias intensity. In this way, the IM proposed here is stated as a generalization of these classical IMs.

Finally, the spectrogram expressing a signal decomposition in terms of time, frequency and spectral power, is plotted in terms of the spectral power expressed in decibels dB , computed as

$$P_{dB} = 10 \log_{10} \left(\frac{P}{P_r} \right) \quad (10)$$

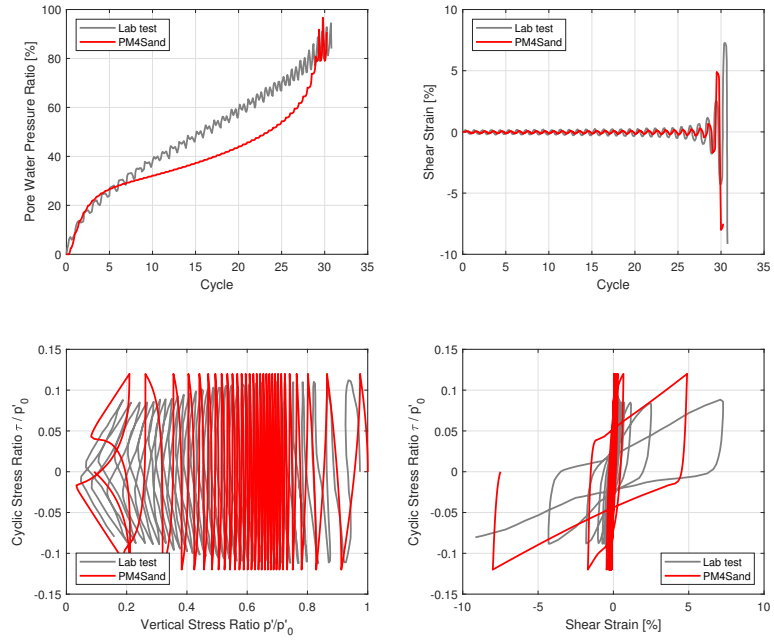
where P is the computed spectral power and $P_r = 10^{1.5}$ is a reference power. The reference power behaves like a simple shift in the accumulated power and does not modify the proposed correlation.

4.2. Application to a set of seismic records

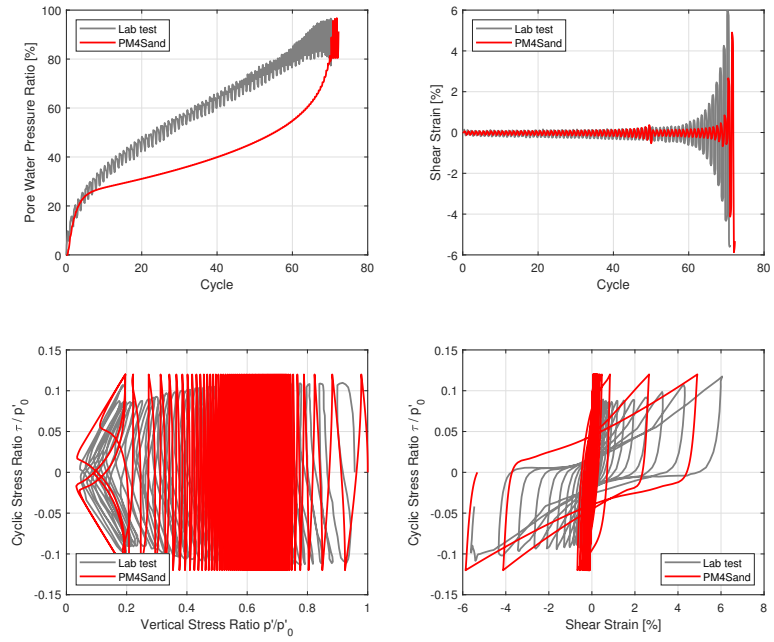
In order to evaluate the liquefaction risk of the TSF described in Section 2, a set of 25 seismic records are selected based on the 85th percentile of the 7500-year event, for which a peak ground acceleration (PGA) of $0.78 g$ is expected. Twenty seismic records correspond to seismographs located on dense soil/soft rock (NEHRP site class C); two (records 3 and 8) belong to firm/hard rock (NEHRP site class B), and three (records 4, 7 and 23) belong to stiff soils (NEHRP site class D). For each seismic record, the acceleration-time signal and spectrogram are computed by using short-time fourier transform [37] and presented in Appendix A, where a Hamming window is used for the calculations. The main characteristics of the records are summarized in Table 4. The spectral power is included together with arias intensity (AI), Cumulative Accelerate Value (CAV) and Cumulative Accelerate Value above $0.05 g$ (CAV5). Spectral power is expressed in relative terms, i.e. the argument of the logarithm, as explained in equation (10).

Figure 6 (a) plots the cumulative spectral power of the seismic records. Some of them have more power at low frequencies; as the frequency window widens, others increase their spectral power. The curves have been organized so that those with higher spectral power in low frequencies are plotted in red, while those with less power are plotted in blue. Seismic records 8, 4, 19 and 7 are those with higher spectral power in the window $0-2 Hz$, while 18, 3, 6 and 1 are the ones with lower power in this range. Another way to express these results is presented in Figure 6 (b) where a mobile Hamming window $2 Hz$ wide is used. It can be seen that some signals like number 9 have power accumulated in medium frequency range, while their content for low and high frequency is relatively low; others like number 8 have higher spectral power in the low band, while the medium and high bands are negligible.

In the following section, it will be demonstrated that the demand of a seismic record on the dam shown in Section 2 is strongly correlated with the spectral power content at low frequencies.



(a) PM4Sand model vs. laboratory tests (N°1)



(b) PM4Sand model vs. laboratory tests (N°2)

Figure 4: Comparison between PM4Sand model and CDSS tests.

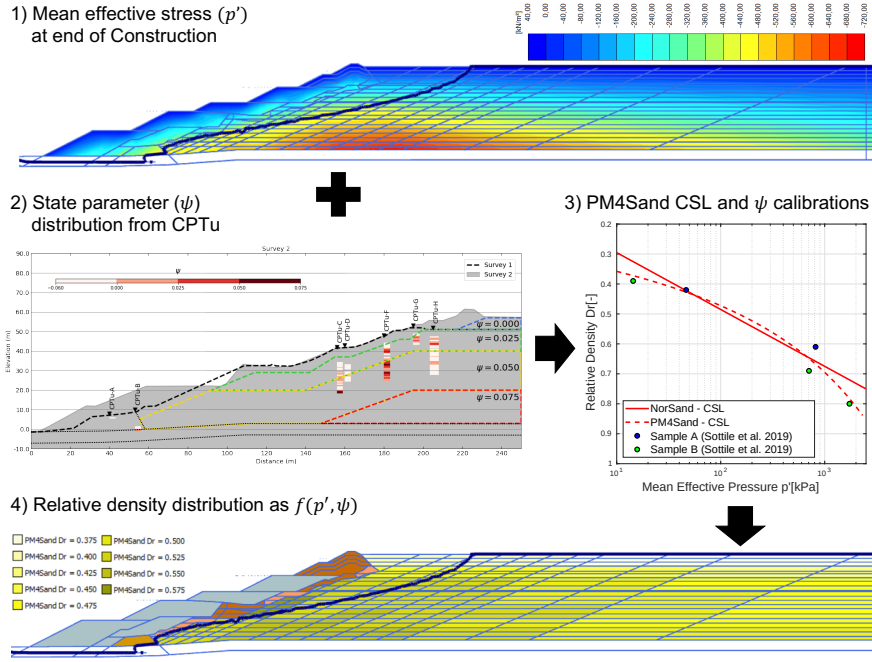


Figure 5: PM4Sand relative density definition strategy.

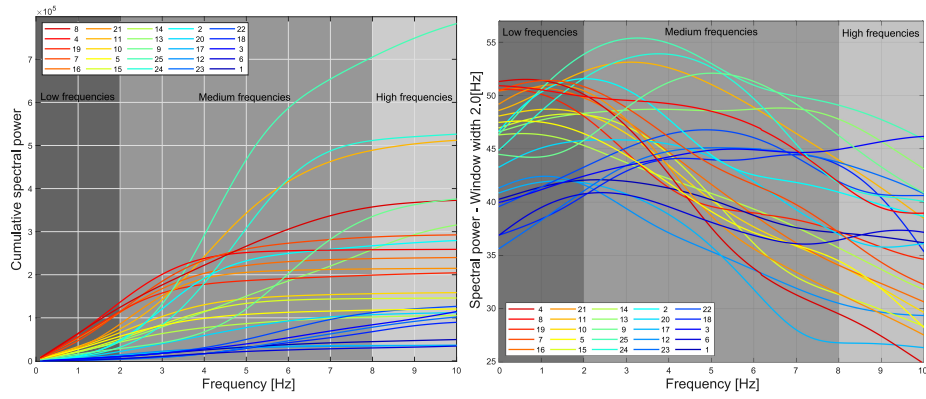


Figure 6: Accumulated spectral power for the considered set of signals, obtained with spectrograms presented in Appendix A.

Table 4: Seismic records used for the seismic analysis, scaled to PGA of 0.78g.

ID	Event Name	Record Station	Duration [sec]	AI [mm/sec]	CAV [mm/sec]	CAV5 [mm/sec]	$\frac{P_{0-1.5 Hz}}{P_r}$ [-]	$\frac{P_{0-2.0 Hz}}{P_r}$ [-]
1	Nahanni Canada	Site 1	10	1931	7337	7340	7021	10627
2	Duzce Turkey	Lamont 375	41	9445	25599	25956	24509	47292
3	Landers	Lucerne	48	7944	26919	26937	7116	9981
4	Kobe Japan	KJMA	150	9057	20488	21410	98654	135265
5	San Salvador	Geotech Inv C.	9	3764	8832	8849	41613	56137
6	Parkfield-02 CA	Parkfield - Cholame 3E	21	1475	5274	5566	2961	4877
7	Chuetsu-oki	Tamati Yone Izumozaki	120	9378	27126	28674	77178	112413
8	Tabas Iran	Tabas	33	11941	30548	31031	95086	124176
9	Iwate	MYG004	300	12444	32509	34949	22159	28378
10	Northridge-01	Jensen Filter Plant Building	29	4947	13887	14166	46433	64496
11	Chi-Chi Taiwan	TCU071	90	16834	44434	44986	49931	71563
12	Mammoth Lakes-06	Long Valley Dam	26	1289	6143	6566	9121	13607
13	Loma Prieta	WAHO	25	11009	26645	26753	32168	45838
14	Victoria Mexico	Cerro Prieto	25	3579	12868	13045	31633	42897
15	Loma Prieta	Corralitos	40	5868	16206	16543	34638	49401
16	Chi-Chi Taiwan	CHY028	90	7677	21532	22451	80261	110293
17	Coalinga-05	Transmitter Hill	22	1205	5174	5558	8452	12217
18	Chuetsu-oki	Joetsu Oshimaku Oka	60	3032	10029	10865	3412	4918
19	C. Mendocino	Petrolia	36	6556	18185	18899	87179	115902
20	Coalinga-05	Oil City	21	3760	8758	8955	13845	21345
21	Chi-Chi Taiwan	CHY041	90	6681	26188	26830	52214	82736
22	Christchurch NZ	LPCC	24	4737	11037	11156	6221	9153
23	N/A	Ward Fire St	164	3749	9307	10112	2422	3830
24	N/A	ANGOL	180	17082	66227	68397	17876	30719
25	N/A	PICA	252	27110	67414	69258	24022	43339

Equation (9) is a generalization of classical seismic intensity measures, filtering the power of frequencies that just brings scatter to correlations. It will be shown that this spurious power in the case of the tailings dam shown as example is that at medium-high to high frequencies (above 5 Hz). Figure 7 shows the comparisons AI in Fig. 7 (a) and (b), proving that Parseval's theorem is accomplished. Fig. 7 (c) to (f) show CAV and CAV5 with cumulative spectral power within different ranges of frequencies. When the band frequency is narrow, i.e. up to 2 Hz , a considerable scatter is found among the intensity measures in all cases but, as the frequency band becomes wider, the accumulated spectral power tends to represent AI, CAV and CAV5 obtaining a perfect fitting in all cases. It is worth noting that for some records like 21 or 24, the filtering produced by CAV and CAV5 does not represent a straightforward energy generalization.

5. Numerical validation

This section presents the validation of the spectral power intensity measure for three types of analyses: Newmark-type rigid block displacement, time-history deformation models using HS-Small (representative of industry-standard analyses) and time-history deformation models using PM4Sand model (aiming at taking into account dynamic liquefaction susceptibility of the tailing).

5.1. Correlation with a Newmark-type model

First, the proposed intensity measure is contrasted with the Newmark displacement [16], a widely-used damage indicator [38, 39, 40, 41]. Relevant parameters presented in Table 3 have been used in all cases.

Correlation between Newmark displacement and some IMs are presented: Arias Intensity in Fig. 8 (a), CAV in Fig. 8 (b), CAV5 in Fig. 8 (c), cumulative spectral power $P_{0-1.0\ Hz}$ in Fig.8 (d), $P_{0-2.0\ Hz}$ in Fig. 8 (e) and finally $P_{0-5.0\ Hz}$ in Fig. 8 (f).

When classical intensity measures are used, an $R^2 = 0.60$ is obtained for the best estimator (AI). Results improve considerably for the proposed intensity measure, where the fitting arises to $R^2 = 0.81$ when the spectral power is accumulated in the window 0 – 5.0 Hz , confirming that, at least in this case, the higher demand correlates with higher power content in low and medium to low frequency ranges.

5.2. Comparison with time-history deformation models using HS-Small

In this section, the configuration and materials of the model are those used for simulating the construction sequence. HS-Small is unable to generate excess pore pressure due to cyclic loading, and therefore this exercise is representative of many problems where seismic liquefaction is not relevant. Two points were selected to quantify the demand induced by each seismic record in terms of

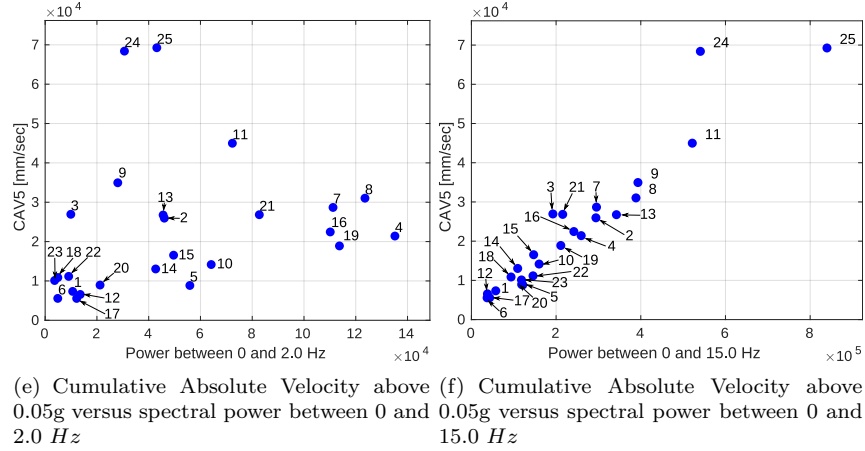
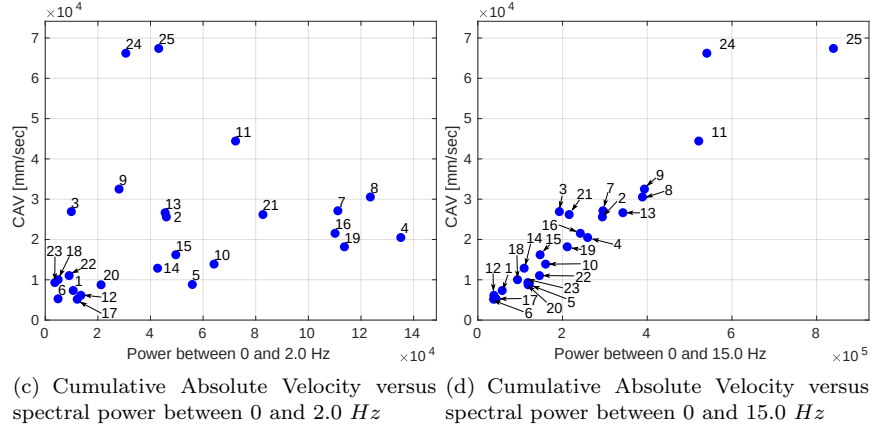
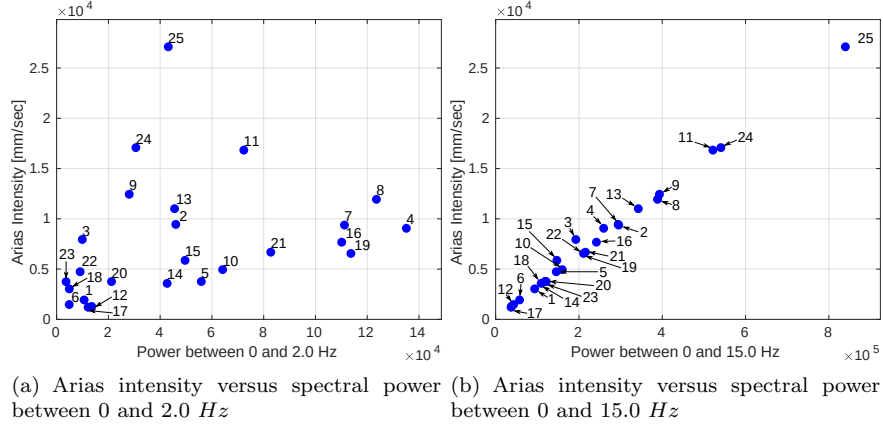


Figure 7: Comparison of the proposed intensity measure based on spectral power and classical IMs.

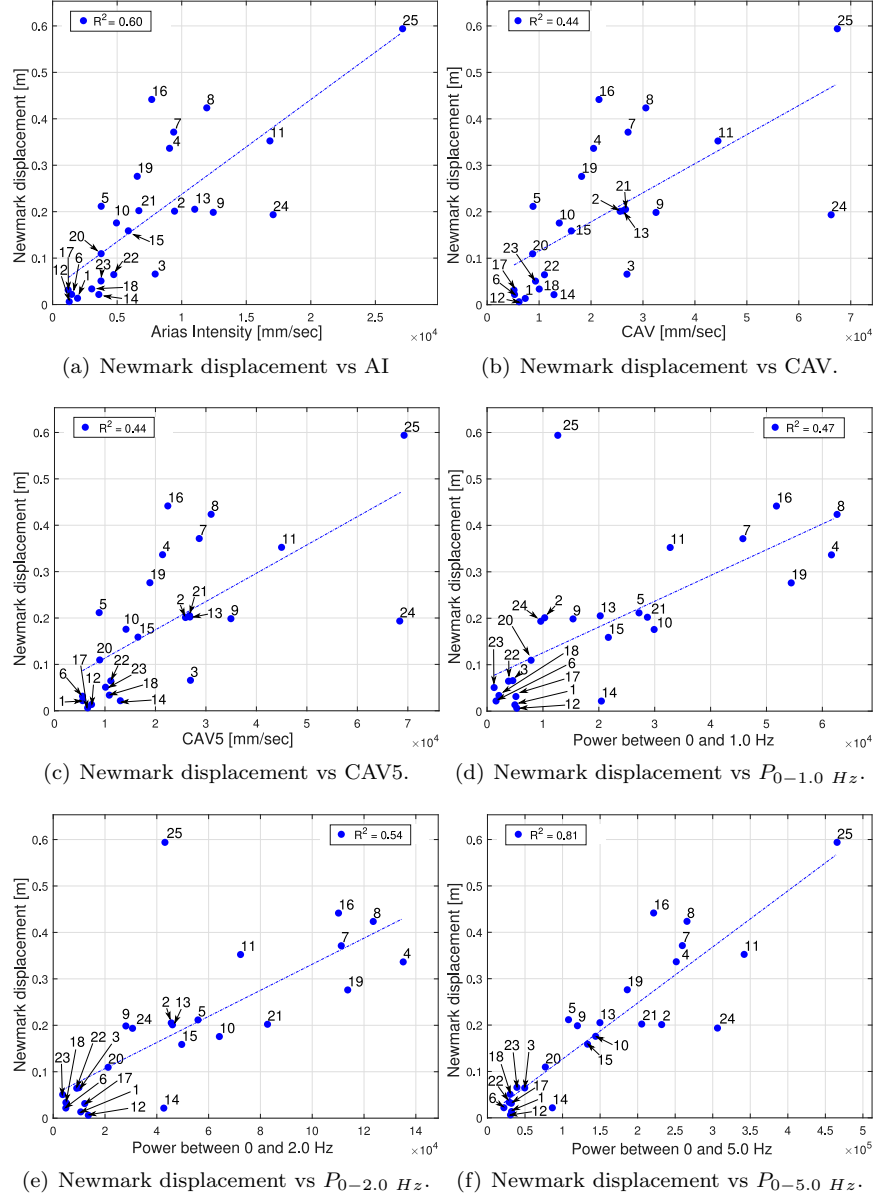


Figure 8: Newmark displacement compared with classical and the proposed intensity measures.

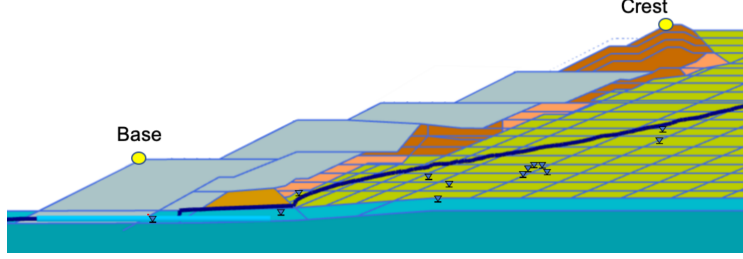


Figure 9: Selected point to measure the displacements in the buttress.

displacement: one in the crest and one in the base of the buttress (see Figure 9).

Figure 10 shows the results of the various IMs, compared with the crest displacement. Correlations for classical IMs are rather poor. The best fit is again obtained by AI with a $R^2 = 0.19$ in Fig. 10 (a). Results for CAV and CAV5 are presented in Fig. 10(b) and (c) respectively. When the spectral power is used, the correlation becomes much better. In this case, the best fit is obtained when the spectral power is accumulated between 0 and 2.5 Hz, i.e. $P_{0-2.5 \text{ Hz}}$ where the $R^2 = 0.86$ as shown in Fig. 10 (e). It is again observed that seismic records with high power in the low and medium-low frequency range produce higher demands.

Similar results are obtained for base displacements. Figures 11 (a) to (c) show base displacements compared with AI, CAV and CAV5 respectively, showing a best fit for AI with an $R^2 = 0.22$. Figure 11 (d) shows the correlation with $P_{0-2.5 \text{ Hz}}$, obtaining a better fit.

5.3. Comparison with time-history deformation models using PM4Sand model

The exercise is repeated using PM4Sand model, and can be considered representative of problems where seismic liquefaction must be studied for contractive and saturated materials. Figure 12 shows the displacement map produced by each seismic record. Results have been organized into groups of small (SD), moderate (MD) and large displacements (LD). In some cases, like records 1 to 3, damage is negligible with displacements concentrated on the edge of the buttress. Records 4, 8, 16, 19, 21, among others, produce a considerable damage with a huge portion of tailings sliding down due to liquefaction.

Figures 13 (a) to (c) shows the time history of the base displacements, while Figures 13 (d) to (f) shows the time history at the crest. Apparently, there is no correlation, as the scatter is very high for all IMs.

Attention must be given to the results of seismic records N°9 and N°4 to prove the novelty of the method proposed in this paper. Figure 14 shows the spectrograms of the aforementioned signals, where the corresponding to N°9 shows that most of its power is concentrated in high frequencies, while the

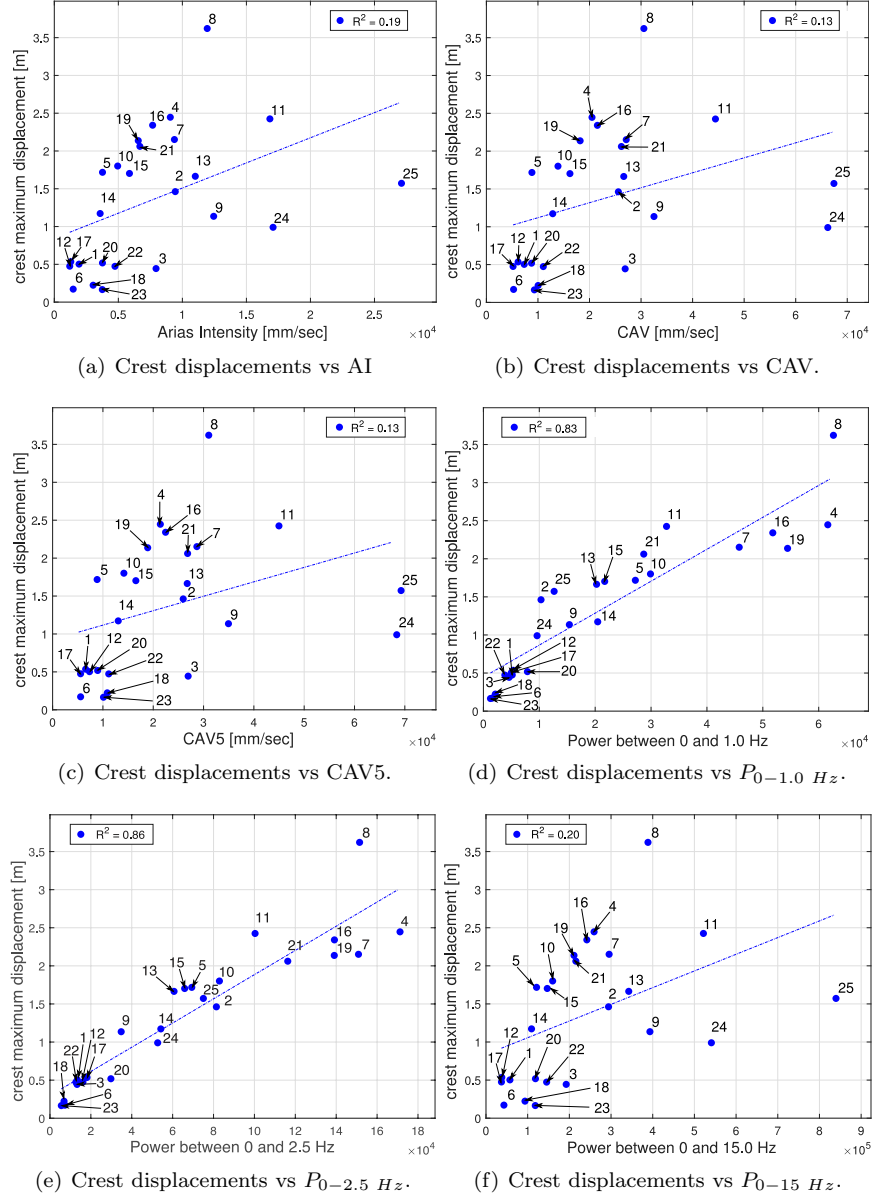


Figure 10: Crest displacements obtained with the Hardening Soil Small (HS-Small) model compared with classical and the proposed intensity measures.

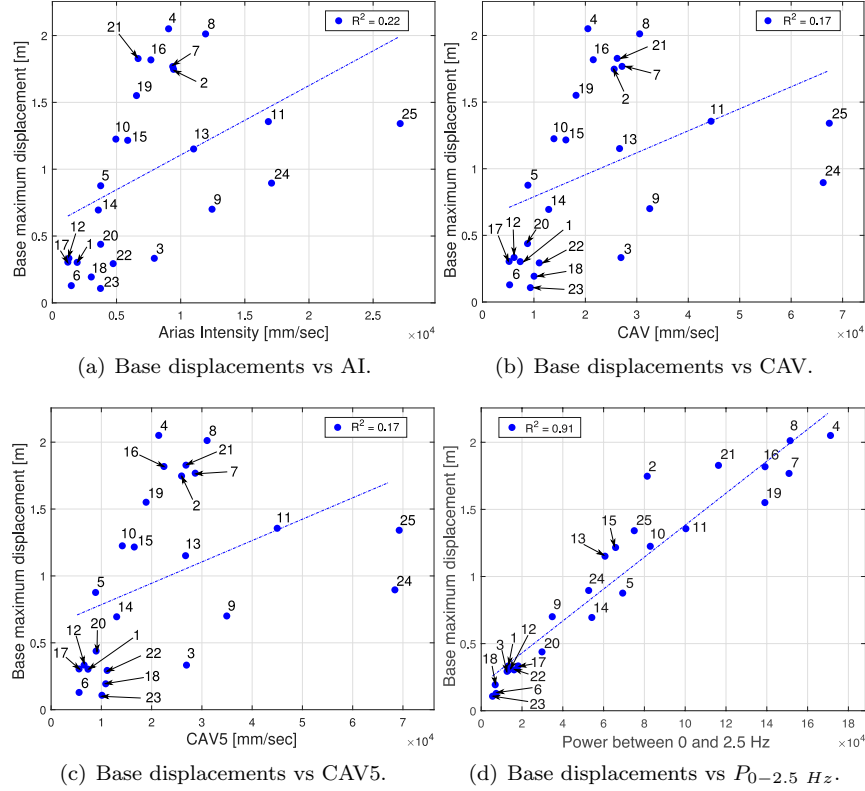


Figure 11: Base displacements obtained with the Hardening Soil Small model compared with classical and the proposed intensity measures.

spectrogram for record N°4 shows exactly the opposite, with most of the energy in the low frequency range.

If demand were to correlate with Arias Intensity, record N°9 should be the most demanding but, as shown in Figure 15, the most demanding is N°4. This phenomenon is captured by the intensity measure expressed in terms of spectral power, being the power concentrated in low frequencies higher in ground motion which produces higher demand.

Figure 16 shows the maximum time-history displacement obtained for different seismic intensity measures. Similarly to the results obtained for the Newmark and HS-Small exercises, poor results are obtained with classical IMs, and the best fit is the one with AI, with a $R^2 = 0.07$ in Figure 16 (a), while for CAV and CAV5 in Fig. 16 (b) and (c) respectively, the correlation is even worse. The spectral power intensity measure presented in Fig. 16 (d) shows an excellent fit with an $R^2 = 0.95$ when low frequencies are considered, i.e. $P_{0-2.0 \text{ Hz}}$. When the frequency band becomes wider, the scatter increases

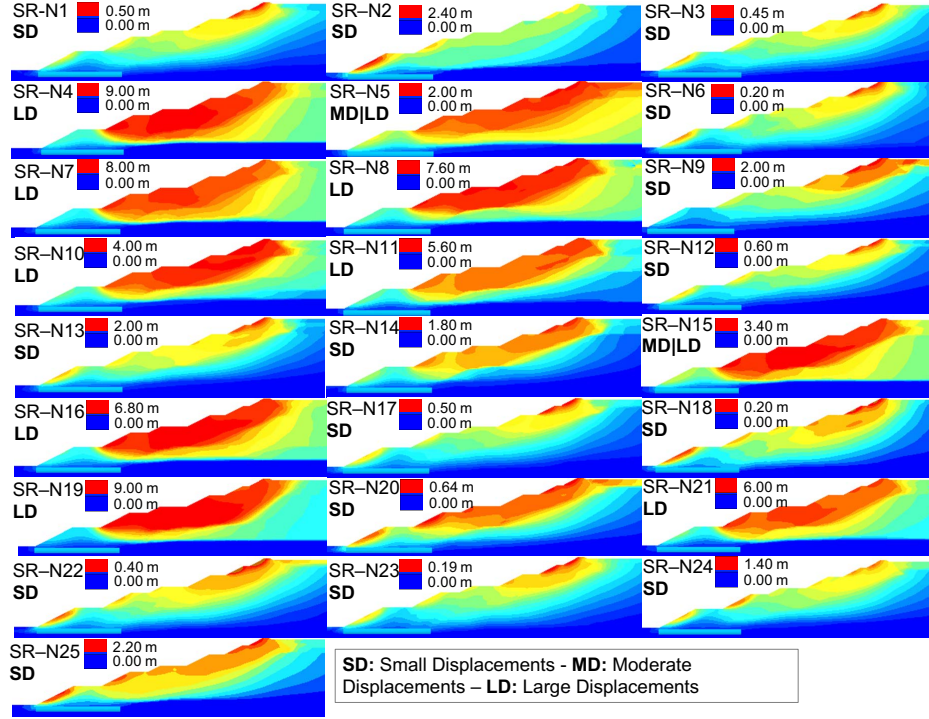


Figure 12: Map of displacements obtained for each seismic record using PM4Sand model.

obtaining a similar pattern than the one obtained for the AI (Fig. 16 (e)).

The best width of the window of the spectral power IM must of course depend on the problem in hand. In the example shown here, the fundamental frequency of the tailings body was computed in Section 2 to be $f_1 = 0.70 \text{ Hz}$, yielding a fundamental period of $T = 1.43 \text{ s}$, which suggests that, at least in this case and maybe in similar analyses, a window width of $0 - 2.0 T$ would be a good starting point to use the proposed IM as a tool to make a priori estimates of the seismic demand that a given record would produce to the dam under study.

6. Conclusions

A novel intensity measure (IM) based on the spectral power of seismic records has been presented and applied to the problem of estimating the displacement demand of an upstream-raised tailings storage facility (TSF) subjected to strong earthquakes. The proposal is inspired by the evidence that the seismic demand of such TSFs -base and crest displacement- is strongly correlated with the power of the earthquakes at low and medium-low frequency range, close to the first-mode natural period of the dams.

The numerical model set up for the dynamic deformation analysis of a large TSF has been briefly described as an example, including the calibration of HS-Small and PM4Sand constitutive models. The mathematical definition of the proposed intensity measure based on spectral power has been introduced in a discrete domain, detailing the equations required to perform the computations.

It has been shown that the proposed intensity measure based on the spectral power is as generalization of other classical and well-known intensity measures such as Arias Intensity, Cumulative Absolute Velocity and Cumulative Absolute Velocity above $0.05\ g$, and that it provides a better correlation with seismic demand of the dam for three design procedures used as examples: Newmark-type displacement analysis, time-history deformation analysis using HS-Small and time-history deformation analysis using PM4Sand model. It has been demonstrated that the key aspect to be accounted for is the filtering of spectral power in the frequency band relevant to the structure under analysis.

In the example shown, where the fundamental period is $T = 1.43\ s$, the correlation between the spectral power intensity measure and seismic demand was $R^2 = 0.81$ for the Newmark-type analysis, $R^2 = 0.86$ for the HS-Small deformation modeling and up to $R^2 = 0.95$ for the PM4Sand deformation modeling. The best frequency window has a slight dependence on the calculation method, but for all cases frequencies belongs to a low range, being $0 - 5.0\ Hz$ to the Newmark case, $0 - 2.5\ Hz$ for the HS-small model and $0 - 2.0\ Hz$ for the PM4Sand model. It was suggested that a window width of $0 - 2.0\ T$ would be a good starting point to use the proposed IM as a tool to make a priori estimates of the seismic demand that a given record would produce to the dam under study.

References

- [1] R. C. Bachus, M. Terzariol, C. Pasten, S. H. Chong, S. Dai, M. S. Cha, S. Kim, J. Jang, E. Papadopoulos, S. Roshankhah, L. Lei, A. Garcia, J. Park, A. Sivaram, F. Santamarina, X. Ren, and J. C. Santamarina. Characterization and engineering properties of dry and ponded class-f fly ash. *Journal of Geotechnical and Geoenvironmental Engineering*, 145(3):04019003, 2019.
- [2] J. Carlos Santamarina, Luis A. Torres-Cruz, and Robert C. Bachus. Why coal ash and tailings dam disasters occur. *Science*, 364(6440):526–528, 2019.
- [3] M. P. Davies. Tailings impoundment failures: Are geotechnical engineers listening? *Geotechnical News*, 20:31 – 36, 2002.
- [4] M. Rico, G. Benito, A.R. Salgueiro, A. Díez-Herrero, and H.G. Pereira. Reported tailings dam failures: A review of the european incidents in the worldwide context. *Journal of Hazardous Materials*, 152(2):846 – 852, 2008.

- [5] ANCOLD, editor. *Australian National committee on Large Dams. Guidelines on Tailings Dams. Planning, Design, Construction, Operation and Closure*. Australian National Committee on Large Dams, 2019.
- [6] M. G. Sottile, N. A. Labanda, I. A. Kerguelén, A. Cueto, and A. O. Sfriso. Stability assessment of a tailings storage facility using a non-local constitutive model accounting for anisotropic strain-softening. In *Challenges and Innovations in Geomechanics*, pages 334–342, 2021.
- [7] J. D. Bray and T. Travarasrou. Pseudostatic slope stability procedure. pages 1–12, 2011.
- [8] B. Ebrahimian. Non-linear numerical analysis of earthquake- induced deformation of earth-fill dams. *Advances in Geotechnical Earthquake Engineering - Soil Liquefaction and Seismic Safety of Dams and Monuments*. Edited by Abbas Moustafa, Intech Publisher, pages 1–10, 2012.
- [9] A. Arias. A measure of earthquake intensity. *Seismic design for nuclear power plants*. Cambridge, Massachusetts Institute of Technology Press, pages 438–483, 1990.
- [10] Steven L. Kramer and Robert A. Mitchell. Ground motion intensity measures for liquefaction hazard evaluation. *Earthquake Spectra*, 22(2):413–438, 2006.
- [11] R.A. Green, J.K. Mitchell, and C.P. Polito. An energy-based excess pore pressure generation model for cohesionless soils. *Proceedings of the John Booker Memorial Symposium, Sydney, New South Wales, Australia*. A.A. Balkema Publishers, Rotterdam, Netherlands, pages 1–9, 2000.
- [12] S.L. Kramer, S.S. Sideras, and M.W. Greenfield. The timing of liquefaction and its utility in liquefaction hazard evaluation. *Soil Dynamics and Earthquake Engineering*, 91:133 – 146, 2016. 6ICEGE – Earthquake Geotechnical Engineering.
- [13] S.L. Kramer, S.S. Sideras, M.W. Greenfield, and B. Hushmand. Liquefaction, ground motions, and pore pressures at the wildlife liquefaction array in the 1987 superstition hills earthquake. volume 2018-June, pages 384–402, 2018.
- [14] Kristel C. Meza-Fajardo, Chiara Varone, Luca Lenti, Salvatore Martino, and Jean-François Semblat. Surface wave quantification in a highly heterogeneous alluvial basin: Case study of the fosso di vallerano valley, rome, italy. *Soil Dynamics and Earthquake Engineering*, 120:292 – 300, 2019.
- [15] P.T. Özener, M.W. Greenfield, S.S. Sideras, and S.L. Kramer. Identification of time of liquefaction triggering. *Soil Dynamics and Earthquake Engineering*, 128:105895, 2020.

- [16] N. M. Newmark. Effects of earthquakes on dams and embankments. *Géotechnique*, 15(2):139–160, 1965.
- [17] Konstantinos Chousianitis, Vincenzo Del Gaudio, Ioannis Kalogeras, and Athanassios Ganas. Predictive model of arias intensity and newmark displacement for regional scale evaluation of earthquake-induced landslide hazard in greece. *Soil Dynamics and Earthquake Engineering*, 65:11 – 29, 2014.
- [18] R.W. Jibson and D.K. Keefer. Analysis of the seismic origin of landslides: examples from the new madrid seismic zone. *Geological Society of America Bulletin*, 105(4):521–536, 1993.
- [19] Randall W. Jibson. Regression models for estimating coseismic landslide displacement. *Engineering Geology*, 91(2):209 – 218, 2007.
- [20] Richard J. Armstrong, Erik J. Malvick, Harpreet Hansra, and Cassidy Eiermann. *Evaluation of Empirical Predictive Models Used to Predict Earthquake-Induced Slope Deformations*, pages 1250–1259.
- [21] Rana Roy, Debasis Ghosh, and Gautam Bhattacharya. Influence of strong motion characteristics on permanent displacement of slopes. *Landslides*, 13(2):279–292, Apr 2016.
- [22] Manya Deyanova, Carlo G. Lai, and Mario Martinelli. Displacement – based parametric study on the seismic response of gravity earth-retaining walls. *Soil Dynamics and Earthquake Engineering*, 80:210 – 224, 2016.
- [23] Mahdi Naeini and Ali Akhtarpour. Numerical analysis of seismic stability of a high centerline tailings dam. *Soil Dynamics and Earthquake Engineering*, 107:179 – 194, 2018.
- [24] R. T. Severn. Dynamic behaviour of arch dams. In José O. Pedro, editor, *Arch Dams*, pages 289–403, Vienna, 1999. Springer Vienna.
- [25] Jin-Hung Hwang, Chia-Pin Wu, and Sheng-Chin Wang. Seismic record analysis of the liyutan earth dam. *Canadian Geotechnical Journal*, 44(11):1351–1377, 2007.
- [26] Jiayu Jin, Chenguang Song, Bing Liang, Yijun Chen, and Menglei Su. Dynamic characteristics of tailings reservoir under seismic load. *Environmental Earth Sciences*, 77(18):654, Sep 2018.
- [27] Kenji Ishihara, Kennosuke Ueno, Seishi Yamada, Susumu Yasuda, and Takeshi Yoneoka. Breach of a tailings dam in the 2011 earthquake in japan. *Soil Dynamics and Earthquake Engineering*, 68:3 – 22, 2015. The Kenji Ishihara Lecture Series Inaugural Articles.
- [28] BAOTIAN XU, QIUSHEN LU, and DONGLIN HE. Seismic Stability Analysis of the Yanghuya Fly Ash Tailings Dam. *Environmental and Engineering Geoscience*, 20(4):371–391, 11 2014.

- [29] Liu Wenlian, Xie Jianbin, Cheng Heming, and d He Tianchun3. Research on the dynamic response of zhuziqing tailings dam. *Applied Mechanics and Materials*, 170-173:1926–1931, 2012.
- [30] Waldemar Świdziński, Aleksandra Korzec, and Kinga Woźniczko. *Stability Analysis of Żelazny Most Tailings Dam Loaded by Mining-Induced Earthquakes*, pages 303–311. Springer International Publishing, Cham, 2016.
- [31] Mohammad Amin Hariri-Ardebili and Jun Xu. Efficient seismic reliability analysis of large-scale coupled systems including epistemic and aleatory uncertainties. *Soil Dynamics and Earthquake Engineering*, 116:761 – 773, 2019.
- [32] M. Hudson, I. Idriss, and M Bourke. Quad4m user’s manual. 1994.
- [33] R.W. Boulanger and K. Ziotopoulou. Pm4sand (version 3.1): A sand plasticity model for earthquake engineering applications. *Report No. UCD/CGM-17/01. Center of Geomechanical Modeling. Department of Civil and Environmental Engineering. University of California, Davis, California*, pages 1–113, 2017.
- [34] M. G. Sottile, A. Kerguelen, and Sfriso A. O. A comparison of procedures for determining the state parameter of silt-like tailings. In Prof. Denis Kalumba, editor, *The 17th African Regional Conference on Soil Mechanics and Geotechnical Engineering*, pages 1–5, Cape Town, South Africa, 2019.
- [35] Dawn Shuttle and Michael Jefferies. Determining silt state from cptu. *Geotechnical Research*, 3(3):90–118, 2016.
- [36] K. Ziotopoulou and R.W. Boulanger. Calibration and implementation of a sand plasticity plane-strain model for earthquake engineering applications. *Soil Dynamics and Earthquake Engineering*, 53:268 – 280, 2013.
- [37] Alan V. Oppenheim, Ronald W. Schafer, and John R. Buck. *Discrete-Time Signal Processing*. 1999.
- [38] Wenqi Du, Duruo Huang, and Gang Wang. Quantification of model uncertainty and variability in newmark displacement analysis. *Soil Dynamics and Earthquake Engineering*, 109:286 – 298, 2018.
- [39] G. Veylon, L.-H. Luu, S. Mercklé, P.-Y. Bard, A. Delvallée, C. Carvajal, and B. Frigo. A simplified method for estimating newmark displacements of mountain reservoirs. *Soil Dynamics and Earthquake Engineering*, 100:518 – 528, 2017.
- [40] Takaji Kokusho. Energy-based newmark method for earthquake-induced slope displacements. *Soil Dynamics and Earthquake Engineering*, 121:121 – 134, 2019.

- [41] Elisabetta Cattoni, Diana Salciarini, and Claudio Tamagnini. A generalized newmark method for the assessment of permanent displacements of flexible retaining structures under seismic loading conditions. *Soil Dynamics and Earthquake Engineering*, 117:221 – 233, 2019.

Appendix A. Seismic Records

This appendix includes the seismic records used for all the simulations presented in this paper, along with its spectrograms, used to compute our intensity indicator. All of them have been downloaded from the PEERS seismic database.

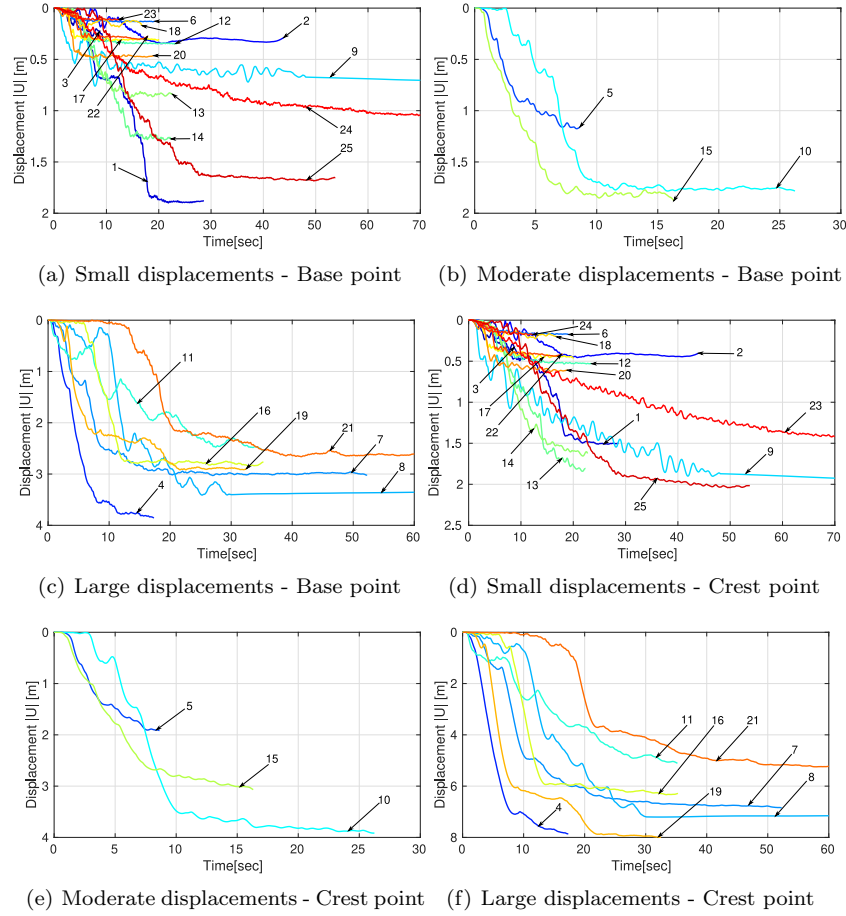
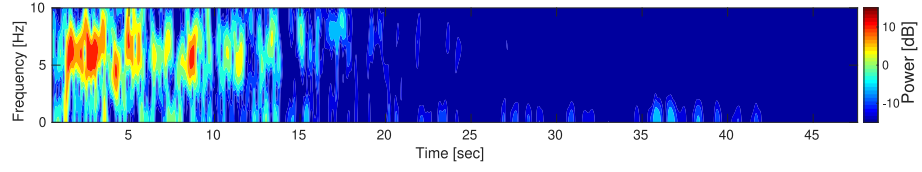
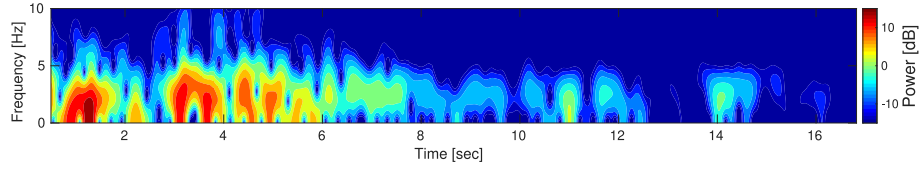


Figure 13: Displacement time-history for base and crest points for all seismic records using PM4Sand model. Large, moderate and small displacements are referred to by colored zones in Figure 16.

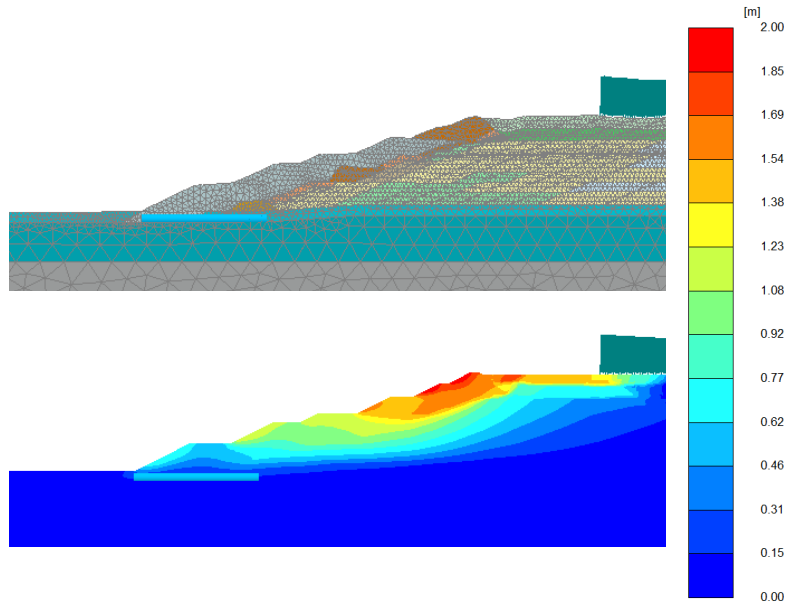


(a) Record N°9 with $AI = 12444$ and $P_{0-2.0 \text{ Hz}}/P_r = 28378.75$.

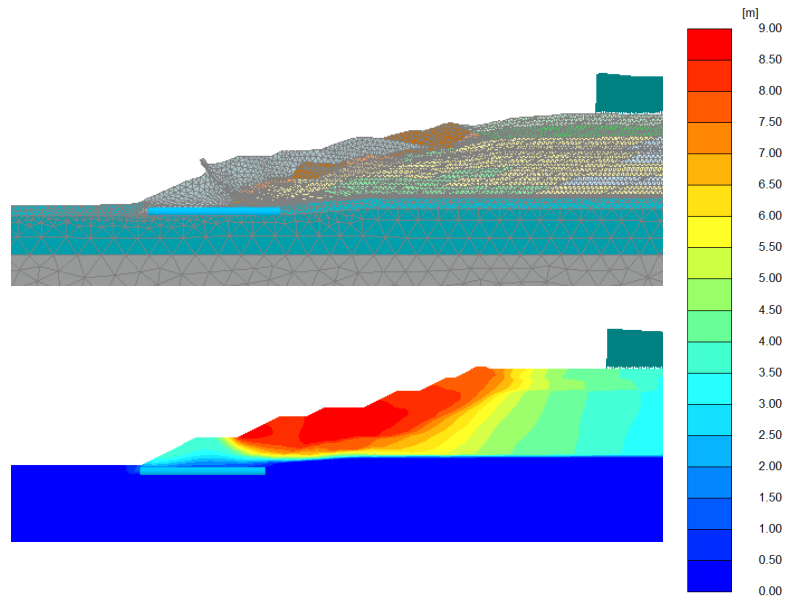


(b) Record N°4 with $AI = 9057$ and $P_{0-2.0 \text{ Hz}}/P_r = 135265.10$.

Figure 14: Three seismic signals inducing different demand levels.



(a) Local deformation for seismic record N°9.



(b) Global failure for seismic record N°4.

Figure 15: Displacement maps obtained for seismic records presented in Figure 14, using PM4Sand model.

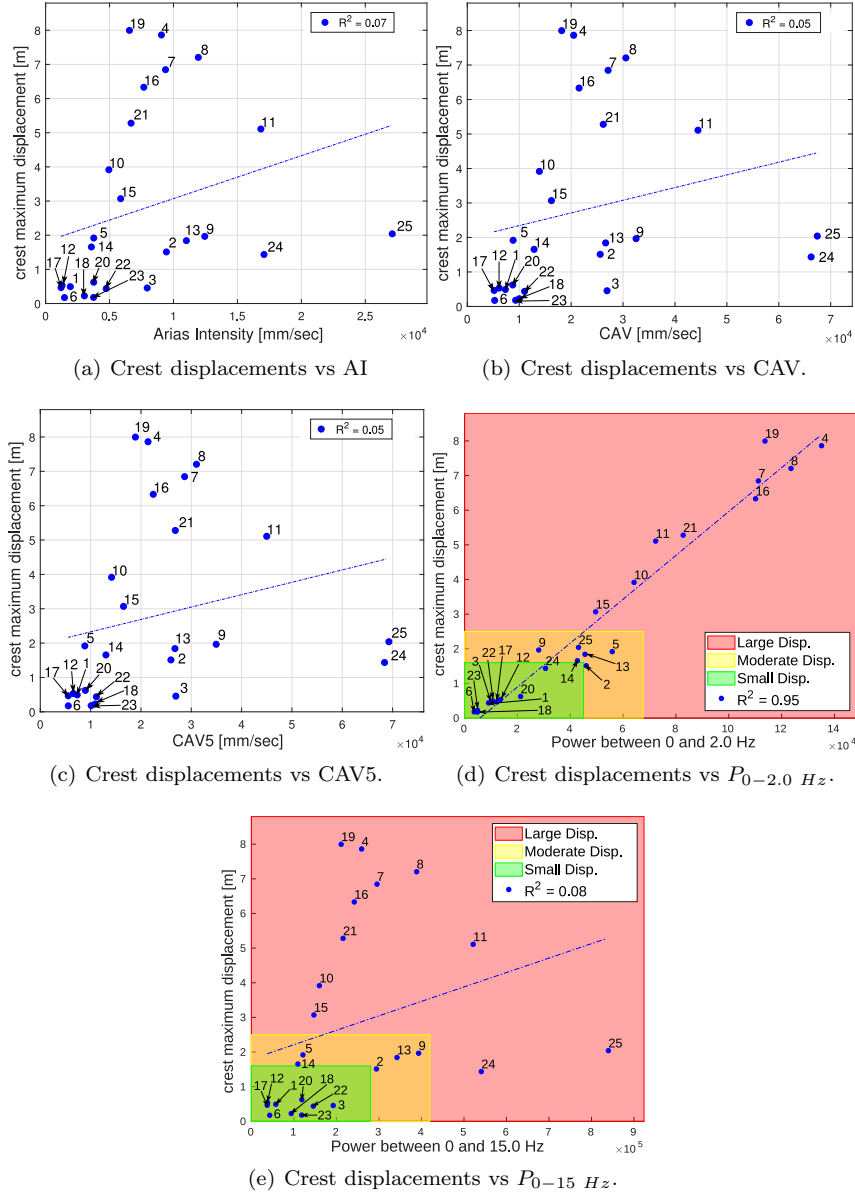


Figure 16: Crest displacements obtained with the PM4Sand model compared with classical and the proposed intensity measure.

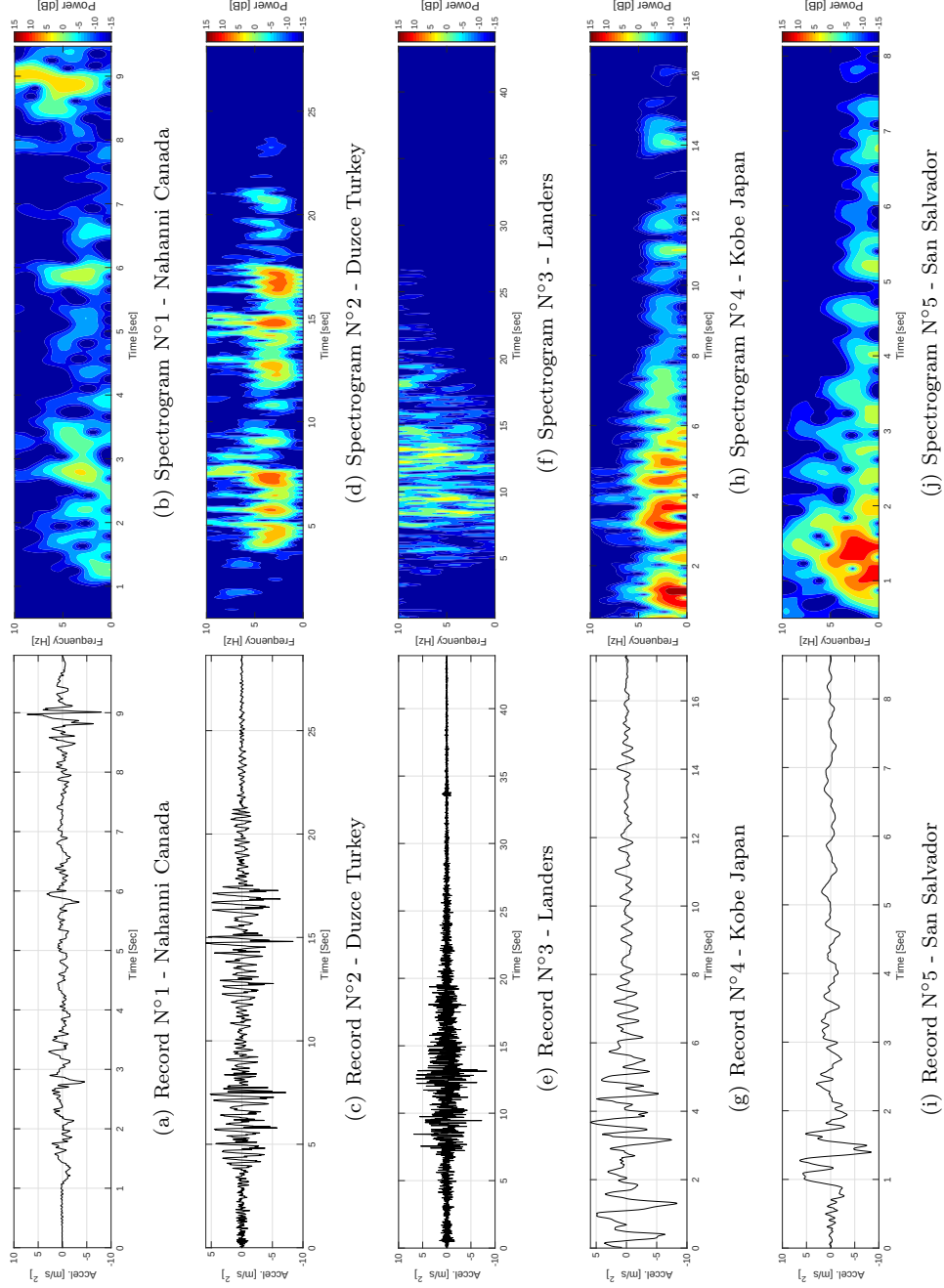


Figure A.16 (cont.): Time history acceleration and spectrograms for considered seismic events.

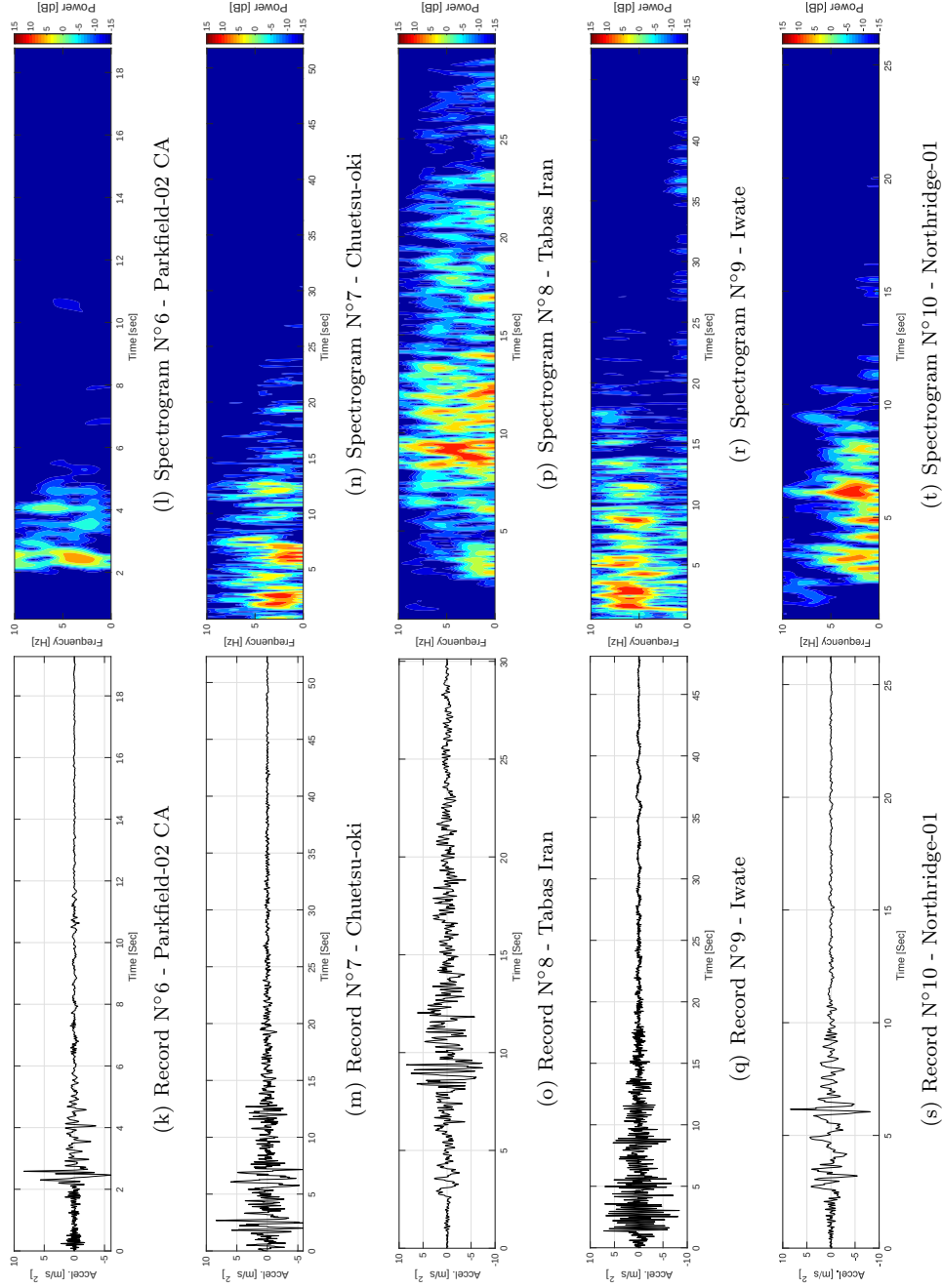


Figure A.16 (cont.): Time history acceleration and spectrograms for considered seismic events.

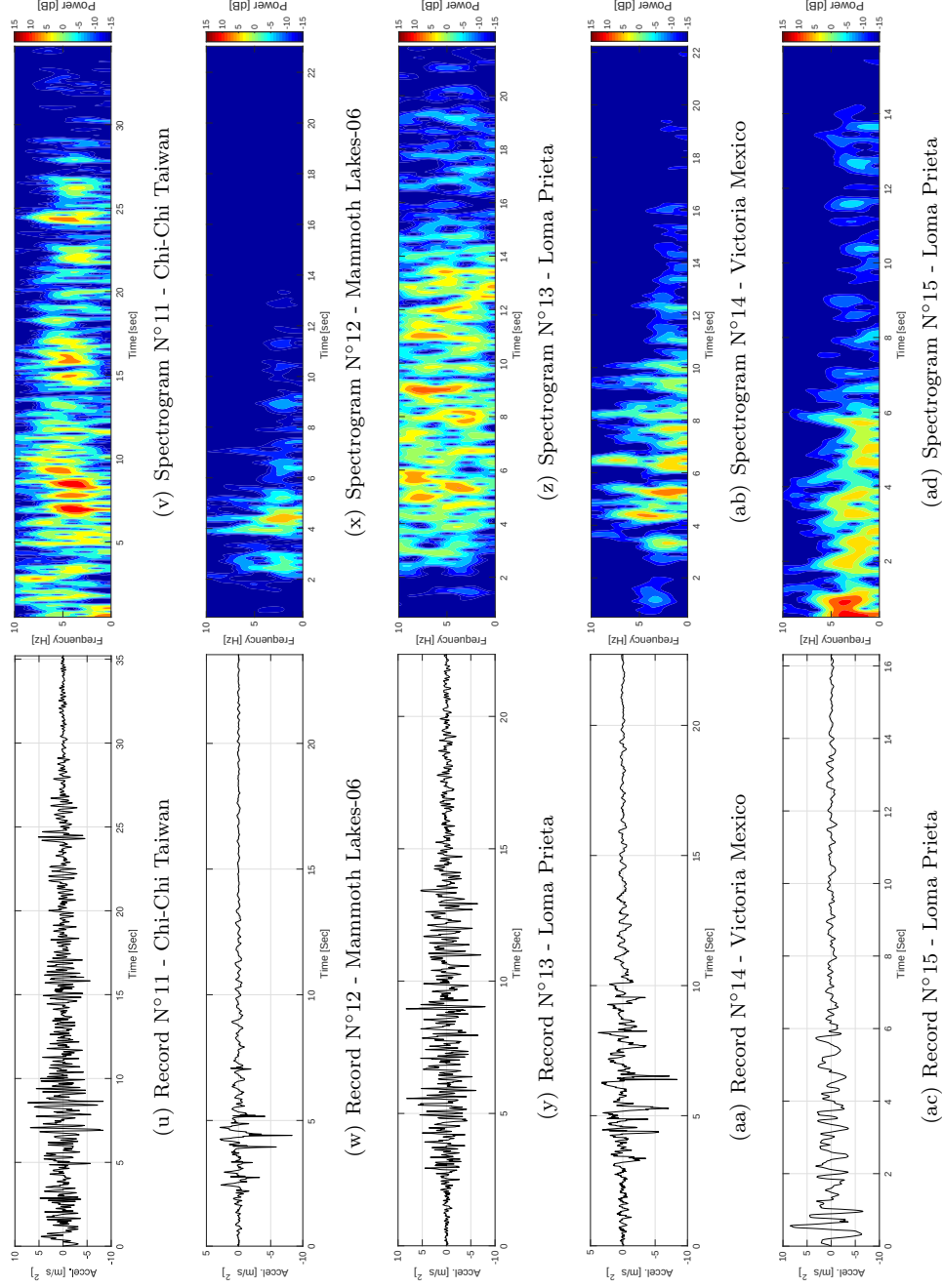


Figure A.16 (cont.): Time history acceleration and spectrograms for considered seismic events.

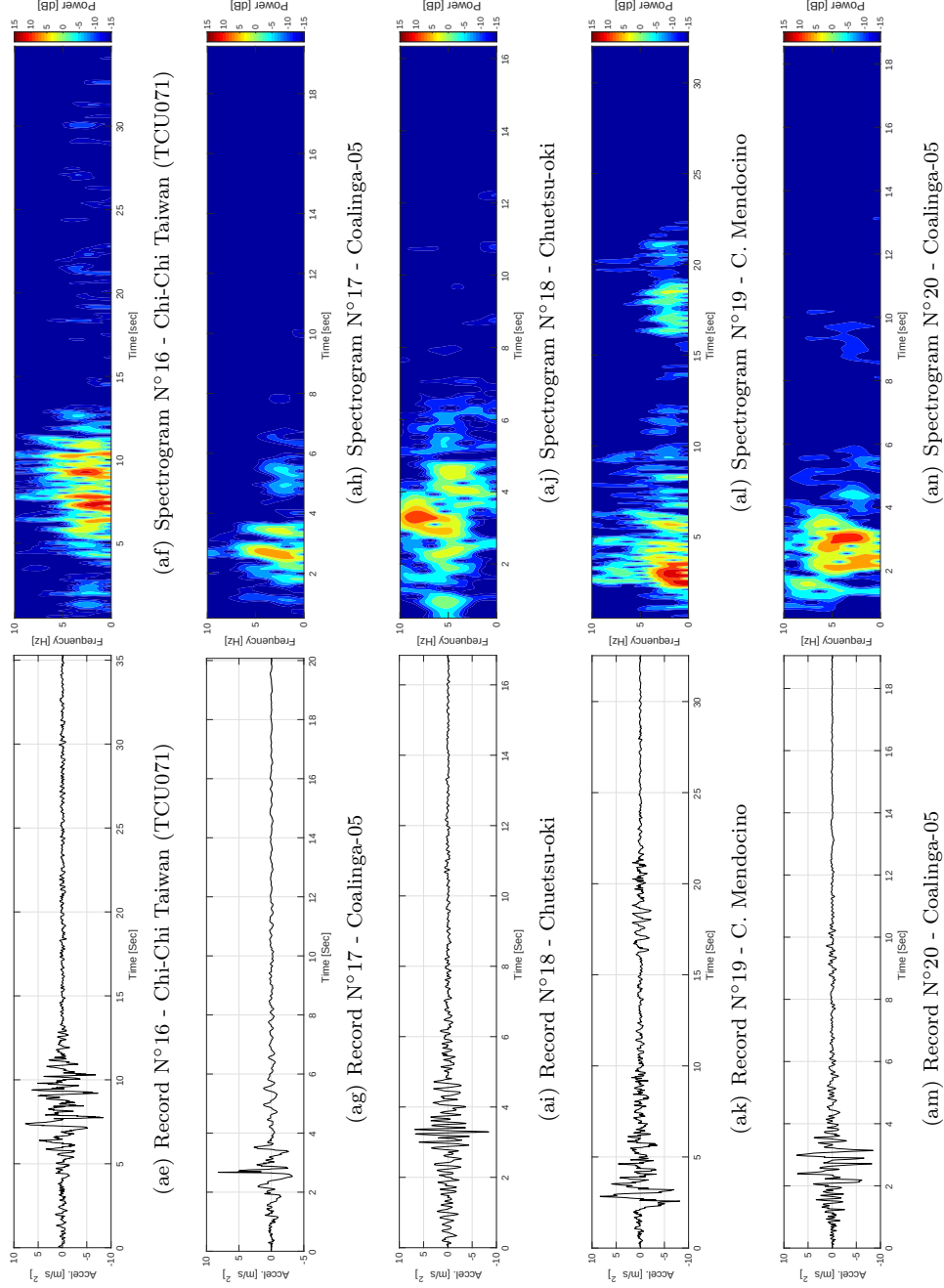


Figure A.16 (cont.): Time history acceleration and spectrograms for considered seismic events.

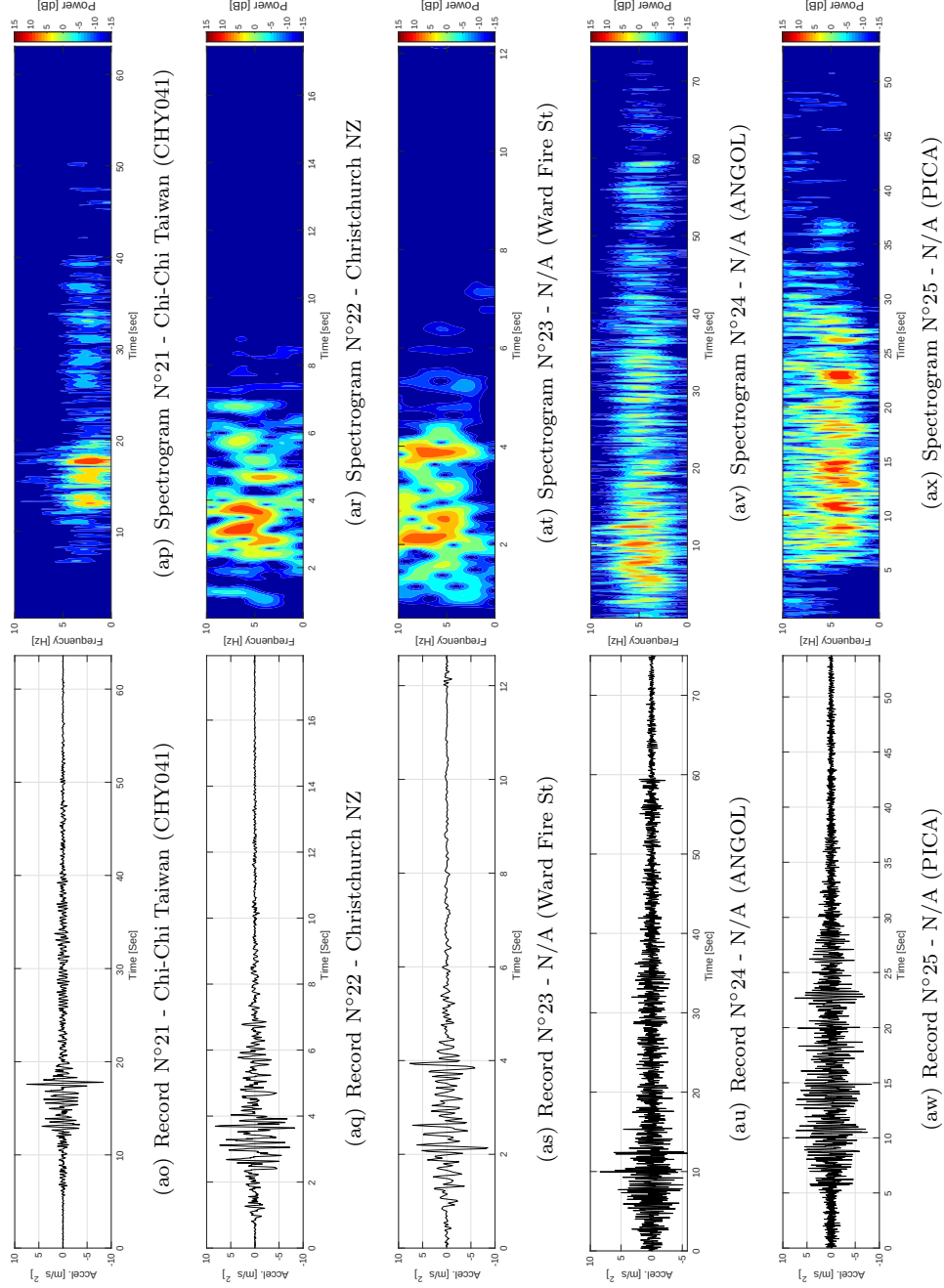


Figure A.16 (cont.): Time history acceleration and spectrograms for considered seismic events.